



Electrochemically synthesized Tin micro-nanometer powders for visible light photocatalytic degradation of Rhodamine B dye from polluted water

Yukun Lu¹ · Yaojie Zhang² · Jiale Zhang¹ · Zhaoyang Li¹ · Feiyang Hu³ · Duo Pan⁴ · Saad Melhi⁵ · Xuetao Shi⁶ · Mohammed A. Amin⁷ · Zeinhom M. El-Bahy⁸ · Qian Shao⁹

Received: 15 April 2024 / Revised: 21 May 2024 / Accepted: 14 June 2024 / Published online: 26 June 2024
© The Author(s), under exclusive licence to Springer Nature Switzerland AG 2024

Abstract

Tin (Sn) micro-nanoparticles with special pine tree dendritic morphology were synthesized by using tin foil as the anode and titanium as the cathode through simple anodization method. Surprisingly, it is found that the morphology of Sn particles is closely related to factors such as the type of electrolyte, the concentration of the electrolyte, and the different applied voltages, and briefly discussed the influence of various factors on the growth of Sn particles. In addition, Sn particles are calcined under different temperature conditions to obtain Sn/SnO₂ hybrid materials with different tin dioxide (SnO₂) contents. The changes in morphology and the phase of SnO₂ crystal lattices were characterized by scanning electron microscopy (SEM) and X-ray diffraction (XRD), respectively, which proved the successful synthesis of Sn/SnO₂ mixed materials. Finally, the Sn/SnO₂ hybrid material with metal-doped modified semiconductor properties was used to photocatalytic degradation of simulated organic pollutants rhodamine B (RhB). It was found that the photocatalytic degradation efficiency of the Sn/SnO₂ hybrid material under simulated sunlight conditions is near 90% in 5 h. Therefore, this work provides a convenient and effective environmental protection approach for the treatment of architecture and industrial dyes.

Keyword Tin micro-nanoparticles · Morphology · Sn/SnO₂ hybrid materials · Photocatalytic activity

1 Introduction

With the increasing awareness of pollutions especially the pollutants such as dyes, heavy metals, etc. in the polluted water [1, 2], more techniques have been developed to remove the pollutants including adsorption, photocatalytic degradation, etc. [3, 4]. Visible light photodegradation has attracted increasing attention and the main part is the effective photocatalysts [5, 6]. Recently, based on their good catalytic activity, tin (Sn) particles have been widely used in catalytic fields such as organic synthesis and redox reaction. [7, 8]. In addition, because of the energy crisis, the development and application of Sn-based materials has become more urgent because of the need for cheap and efficient photocatalysis caused by environmental pollution [9].

Based on the above knowledge, Sn nanomaterials have huge application prospects in many areas of human life, so the research on the preparation of nano-Sn is getting more

and more attention from researchers. Various procedures have been proposed and applied to obtain Sn nanoparticles, such as mechanical alloying technology [10], arc discharge technology [11], metal vapor condensation technology [12], liquid-phase reduction [13], physical vapor deposition (PVD) [14], chemical liquid deposition (CLD) [15], electrochemical method [16], reverse micelle method [17] and so on. For example, Chee et al. [18] used stannous octoate as a raw material, sodium borohydride as a reducing agent, and polyvinylpyrrolidone (PVP) as a surfactant to study the effects of reaction temperature, drying temperature, ultrasonic vibration, and centrifugal speed on the size of Sn nanoparticles. It was found that the size of Sn nanoparticles increased with the increase of reaction temperature and drying temperature, and the agglomeration of Sn nanoparticles was aggravated with the increase of ultrasonic and centrifugal speed [19]. However, in these methods, the Sn nanoparticles obtained by some methods are prone to agglomeration, results in uneven size and contains many impurities (such as mechanical alloying technology and arc discharge technology), some require reaction in a vacuum environment (such as PVD method),

Extended author information available on the last page of the article

and some require harsh experimental conditions and complex operations (such as metal vapor condensation technology) [20–22]. Only the electrochemical method based on electrolysis theory is simple in operation and low in cost, and it is easy to obtain Sn nanoparticles with controllable and uniform morphology by controlling the reaction conditions [23, 24].

In addition, semiconductor oxides play a huge role in the field of catalytic degradation due to their unique electron and hole characteristics [25]. Tin dioxide (SnO_2) as an n-type wide bandgap semiconductor material, which is widely used in the cleaning and purification of organic pollutants in water and air due to its unique photocatalytic activity and good chemical stability [26, 27]. Furthermore, as a photocatalyst, SnO_2 has mild reaction conditions, fast reaction speed, high catalytic activity, strong oxidation ability, low energy consumption, and no secondary pollution, so it is considered to be one of the most promising green catalysts [28–30]. Elango et al. [31] synthesized SnO_2 nanoparticles by green method using *Persia Americana* seed methanolic extract, it was found that the synthesized SnO_2 nanoparticles had a size of 4 nm and exhibited an excellent photocatalytic degradation effect on the organic dye phenolsulfonphthalein (phenol red).

In this paper, Sn particles with a dendritic microstructure were generated at the cathode by a simple electrochemical anodic oxidation method, and then metal Sn-doped semiconductor SnO_2 hybrids with certain photocatalytic activity were obtained by further high-temperature oxidation treatment. With the help of SEM and XRD measurements, the morphologies and structures of the Sn and Sn/ SnO_2 microparticles were characterized respectively. Specifically, the influencing parameters such as applied potential, electrolyte and its concentration were discussed, and the growth of process of Sn microparticles with dendritic structure was also discussed. Different ratio of Sn and SnO_2 in the final product was get after different heat treatment temperature. The final photocatalytic degradation experiment results found that the photocatalytic activity Sn/ SnO_2 particles was superior to that of the pure Sn particles estimated with the degradation of rhodamine B (RhB) under simulated solar light.

2 Experimental procedures

2.1 Materials

High-purity tin flake ($1000 \times 1000 \times 1$ mm, 99.99%) and high-purity titanium flake ($1000 \times 1000 \times 1$ mm, 99.99%) were obtained from Beijing Jinyuan New Material Technology Co., Ltd. (Beijing, China). Ethanol ($\text{CH}_3\text{CH}_2\text{OH}$, 99.7%), acetone (CH_3COCH_3 , AR), isopropanol ($\text{C}_3\text{H}_8\text{O}$, AR) and methanol (CH_3OH , AR) were purchased from Shanghai Aladdin Reagent Co., Ltd., China. Hydrofluoric acid (HF, AR, 40%), nitric

acid (HNO_3 , AR), Ethylenediamine ($\text{C}_2\text{H}_8\text{N}_2$, AR) and ammonium fluoride (NH_4F , AR, 98%) were provided by Shanghai McLean Biochemical Technology Co., Ltd., China. Rhodamine B (RhB) was supplied by Tianjin Bodi Chemical Reagent Co. Ltd. (AR, Tianjin, China). Distilled water was used throughout the experiments. All reagents were of analytical grade and used without further purification.

2.2 Preparation of Sn particles and Sn/ SnO_2 hybrid

Before anodization, it needs to clean and polish the Sn and Ti sheets. Specifically, the Sn sheets and Ti sheets cut into $2 \text{ cm} \times 2 \text{ cm}$ were sonicated in acetone, isopropanol and methanol for 10 min in turn. Then, the Sn sheet was physically polished with sandpaper, and the Ti sheet was chemically polished in a mixture of $\text{V}(\text{HF})\text{:V}(\text{HNO}_3)\text{:V}(\text{H}_2\text{O}) = 1\text{:}4\text{:}5$, and last cleaned with deionized water. Sn particles are obtained through a unique electrochemical method, the experiments were performed at the room temperature in a two-electrodes using Sn plate as the anode and Ti plate as the cathode. The electrolyte used was ethylene glycol solutions of NH_4F which concentration was in the range from 0.04 M to 0.2 M. A constant voltage was applied for each experiment, ranging from 5 to 50 V. After electrochemical reaction for a period of time, the coating deposited on the cathode Ti sheet was collected. The products (Sn particles) were washed and centrifuged several times with distilled water and absolute ethanol respectively to remove the impurities, and then dried in a drying oven at 70°C . The Sn particles are subjected to different high-temperature (450°C , 550°C , and 600°C) oxidation treatments to obtain the corresponding Sn/ SnO_2 hybrid.

2.3 Characterization

The phases and structures of the prepared samples were measured with a Rigaku D/Max2500PC X-ray diffraction (XRD) equipped with graphite monochromatized Cu $\text{K}\alpha$ radiation ($\lambda = 0.15418 \text{ nm}$), using a scanning rate of $4^\circ \cdot \text{min}^{-1}$ in 2θ range from 10° to 80° . The morphology of the products was characterized by a scanning electron microscope (SEM, SU-70) with acceleration voltage of 15 kV. The concentration of RhB in the solution was then measured by using a UV–Vis spectrophotometer (UV9000) at a wavelength of 554 nm.

2.4 Photocatalytic activity performance tests and electrochemical performance analysis

The photocatalytic activity of the product was evaluated through the photodegradation of Rhodamine B (RhB) under a simulated solar light irradiation. The experimental process could be summarized as follows: 0.05 g of the as-prepared samples were dispersed ultrasonically for 2 min in 50 mL

of RhB solution with a concentration of $10 \text{ mg}\cdot\text{L}^{-1}$. A 300 W xenon lamp without any optical filters was employed to simulate the solar light irradiation.

The electrochemical performance (transient photocurrent density) of Sn/SnO₂ hybrid was detected by the three-electrode system of the electrochemical workstation (Autolab, Metrohm Co. Ltd.). Under the intermittent irradiation of xenon lamp to simulate sunlight, a nickel foam (4 cm^2) coated with 20 mg catalyst was used as working electrode, platinum electrode as counter electrode, saturated calomel electrode as reference electrode, and electrolyte selected as 0.1 mol/L Na₂SO₄ solution.

3 Results and discussion

3.1 Morphological characterization of Sn particles obtained under different conditions

Tin (Sn) particles generated at the cathode by electrochemical methods, the morphology and size of Sn microparticles can be controlled by adjusting the experimental conditions, such as composition of electrolyte (fluoride ion content, deionized water content), applied voltage, and reaction time [32–34].

In order to establish the impact of fluoride ion concentration on the micro-nano structure, we prepared samples by changing the NH₄F content (0.04 mol/L, 0.08 mol/L, 0.15 mol/L, 0.20 mol/L, respectively) based on the consistency of other factors (deionized water content of 5 vol%, reaction voltage of 15 V and reaction time of 5 h). As shown in Fig. 1, Sn particles present a unique dendritic morphology, and the shape of the dendrites is closely related to the concentration of NH₄F. From the SEM of Fig. 1a, it can be seen that at low NH₄F content (0.04 mol/L), the obtained dendritic Sn particles are larger in size, the stems are slightly bent, and the whole morphology is rough and irregular. When the concentration of NH₄F increased to 0.08 mol/L, the morphology of dendritic products tended to be regular, the stems tended to be straight and the length of branches decreased (Fig. 1b). When the NH₄F concentration is further increased to 0.15 mol/L, the branches of dendritic Sn particles become finer and the stem length is decreases to 50 μm (Fig. 1c). When the NH₄F content reaches 0.20 mol/L, large-grained dendrites appear, and the dendritic morphology becomes irregular and agglomerated (Fig. 1d). It can be concluded that the content of NH₄F has a great influence on the morphology of tin micro-nano powder, and when its concentration is 0.15 mol/L, the perfect product of Sn dendrite can be obtained.

Next, we analyzed the effect of the content of a small amount of deionized water in the electrolyte solution on the morphology of Sn micro-nanostructures. As shown in Fig. 2a

and 2b, on the basis of other conditions being uniform (NH₄F content of 0.15 mol/L, reaction voltage of 15 V and reaction time of 5 h), at low deionized water content (1.5 and 3 vol%), the dendritic Sn particles are irregular in shape and accompanied by many debris. When the deionized water content increased to 5 vol%, the crystal morphology of the obtained dendritic products tends to be regular and perfect, and the fine branches become numerous and dense (Fig. 2c). When the deionized water content is further increased to 10 vol%, the stem length of dendritic Sn particles increases, but the fine branches tend to be sparse (Fig. 2d).

For the electrochemical reaction process, the applied voltage also has a great influence on the morphology of the deposited product on the electrode [35, 36]. Figure 3 is the SEM of Sn microparticles obtained under different reaction voltages, from Fig. 3a, after 5 h electrochemical reaction, the products obtained by applying a voltage of 5 V are mostly granular, and the dendritic morphology is not perfect. When the applied voltage increased to 10 V, the morphology of dendritic products gradually formed, but the thin branches are not completely bifurcation (Fig. 3b). As the voltage continues to increase to 15 V and 30 V, it can be seen from Fig. 3c and d that the morphology of dendritic Sn particles tends to be regular, and there is no obvious change in the SEM of 15 V and 30 V.

The growth process of Sn microparticles with dendritic structure was studied by controlling the reaction time. In order to explore the crystal growth of Sn particles, the growth process of the crystal product is studied from the nanometer size in a short time (5 min, 30 min, 60 min and 90 min). Under the condition of an applied voltage of 15 V, after the electrochemical reaction for 5 min, the Sn nanoparticles deposited on the cathode show a nano-dispersion state, and the Sn particle size is about 25 nm (Fig. 4a). When the reaction time reaches 30 min, the Sn nanoparticles grow to about 100 nm, but remain independent from each other (Fig. 4b). From Fig. 4c, as the reaction time is above 60 min, Sn nanoparticles grow further and some begin to connect and merge with each other. With the time increased to 90 min, for Sn nanoparticles with increasing size, the compatibility phenomenon is more obvious and the dendritic rudiment appears (Fig. 4d). Until the reaction time increases to 5 h, the Sn particles show a perfect dendritic morphology.

3.2 Mechanism of electrochemical method to generate Sn particles

Combining the growth morphology of Sn crystal products under different conditions above, and based on the theoretical basis for the preparation of metal particles by the electrochemical anodic oxidation-cathode precipitation method, we get that the formation mechanism of Sn particles is mainly divided into four stages.

Fig. 1 SEM images of Sn microparticles obtained with different NH_4F concentration (a) 0.04 mol/L, (b) 0.08 mol/L, (c) 0.15 mol/L and (d) 0.20 mol/L

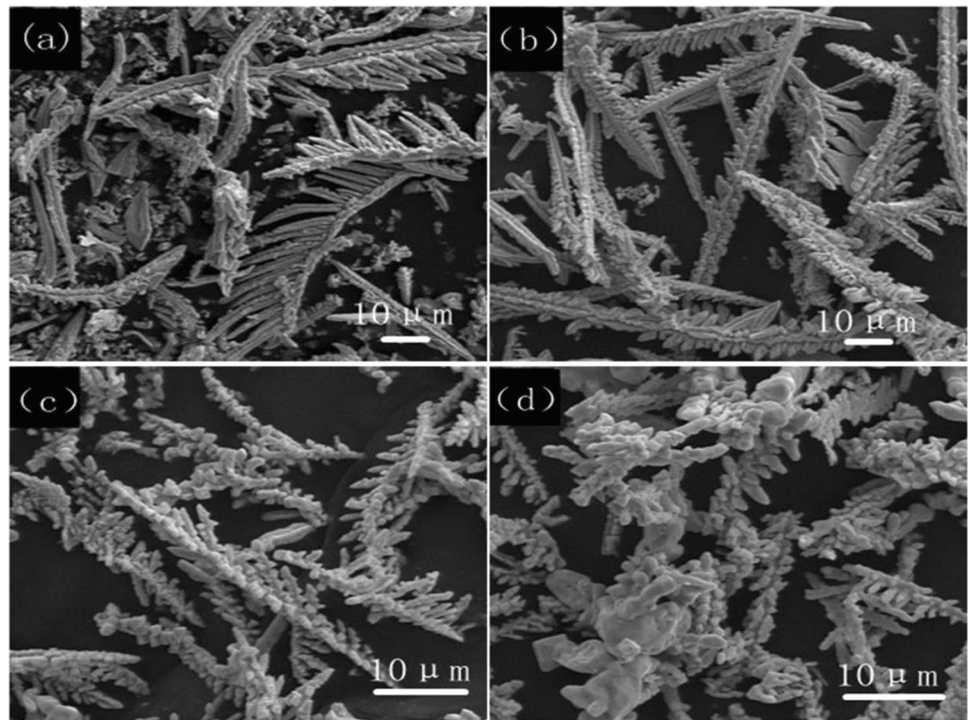
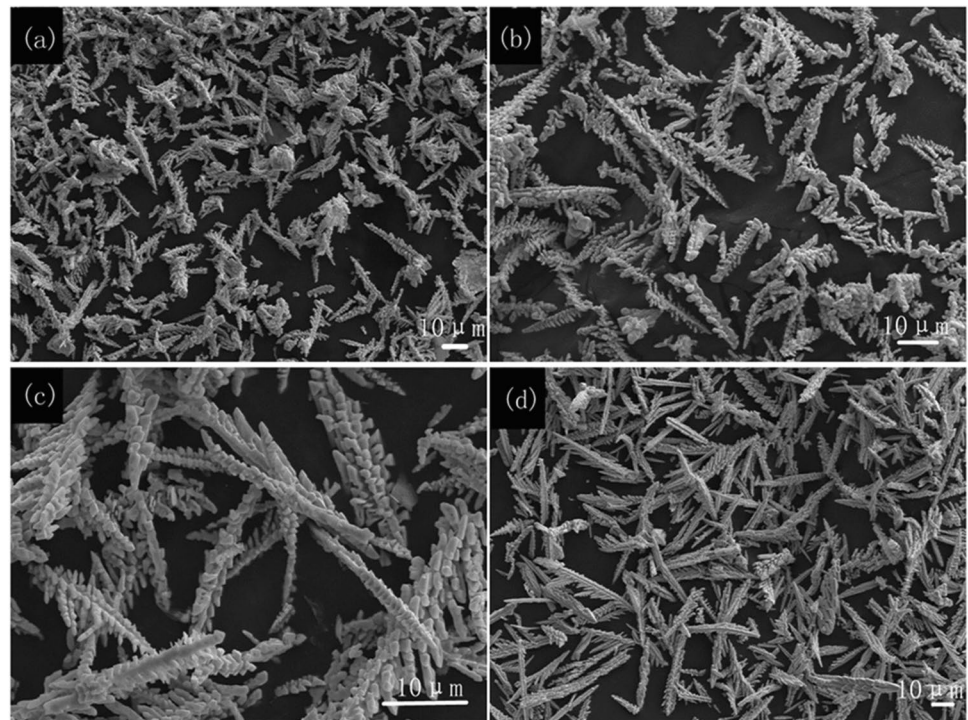


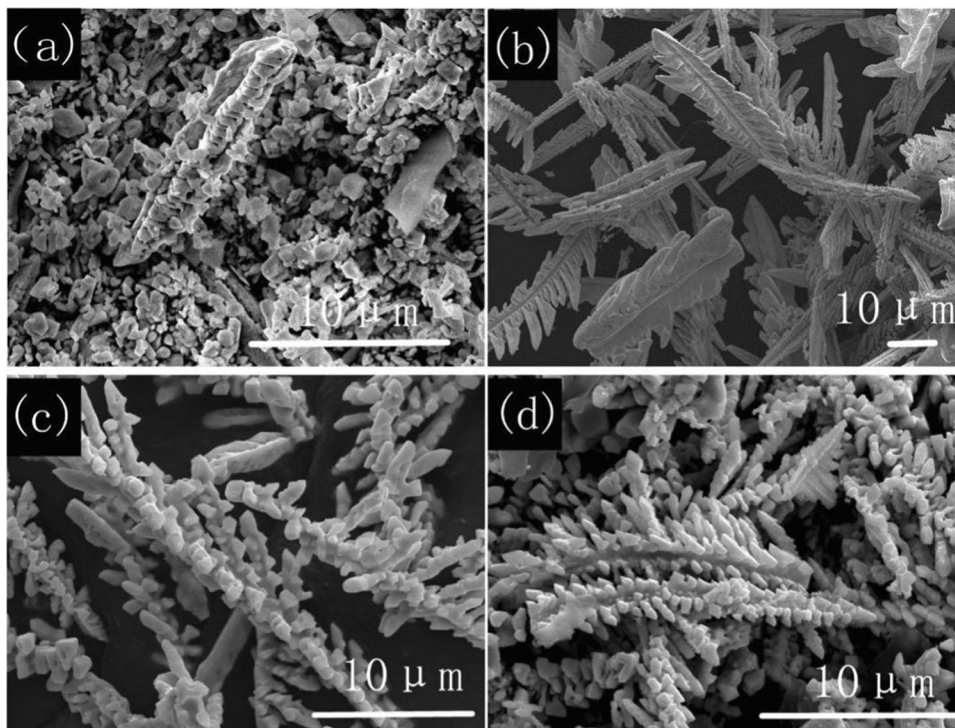
Fig. 2 SEM images of the Sn microparticles prepared with different deionized water content (a) 1.5 vol%, (b) 3 vol%, (c) 5 vol% and (d) 10 vol%



In the first stage, due to the hydrolysis of NH_4F , the electrolyte is weakly acidic, during the electrolysis process [37], the Sn sheet as anode is oxidized, and many micro bubbles appear on the cathode Ti sheet. The main reactions of the two electrodes are as follows:



Fig. 3 SEM images of Sn microparticles prepared using different applied voltage (a) 5 V, (b) 10 V, (c) 15 V and (d) 30 V



In the second stage, the fluoride ion (F^-) in the electrolyte solution is complexed with the tin ion (Sn^{2+}) generated by the anode to obtain SnF_4^{2-} , and the specific reaction is:



In the third stage, the SnF_4^{2-} reach the vicinity of the cathode under the action of magnetic stirring and are reduced to metal Sn particles by obtaining electrons, the reaction is as follows:



In the fourth stage, when the metal Sn crystal nucleus starts to precipitate on the cathode, as the reaction proceeds, the Sn particles gradually grow and become larger in size, and with the different reaction conditions, the morphology of the obtained Sn particles is also different.

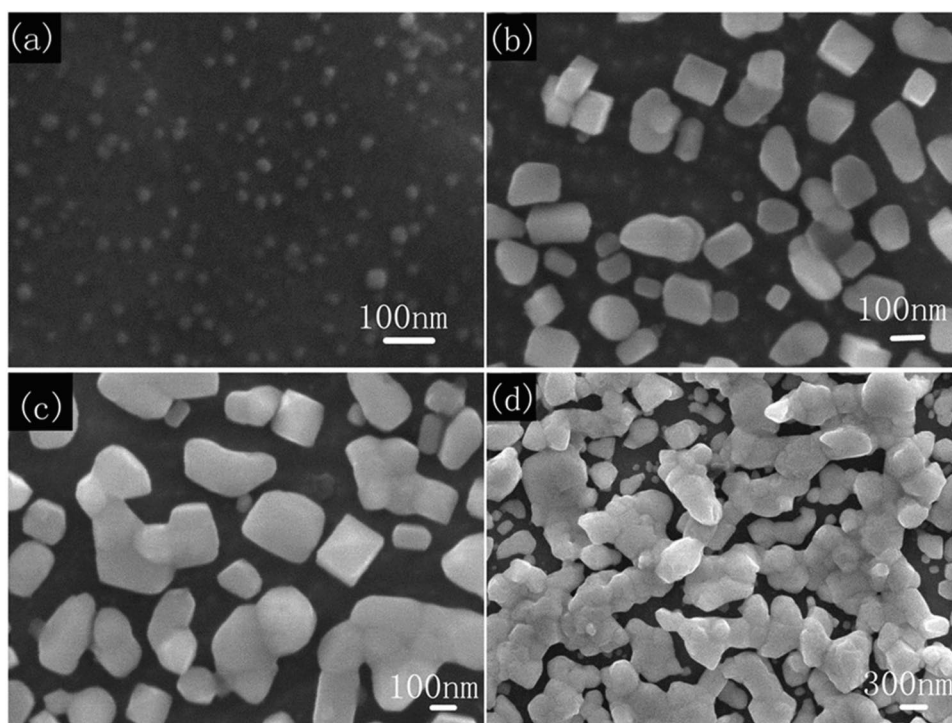
3.3 Characterization analysis of Sn/SnO₂ after Sn particles treated at different high temperatures

By exploring the influence of different conditions on the crystal morphology, the optimal conditions for the electrochemical method to prepare Sn particles are obtained: in the ethylene glycol electrolyte solution containing NH_4F , the content of NH_4F is 0.15 mol/L, the deionized water content was 5 vol%, and the reaction is carried out for 5 h under the applied working voltage of 15 V. In order to make the product have higher

photocatalytic activity, the Sn particles with dendritic crystal morphology were then subjected to high-temperature calcination treatment at 450 °C, 550 °C and 600 °C, respectively [38, 39], and the SEM of the obtained samples are shown in Fig. 5a-c. Compared with the Sn particles, the morphology of the samples changed after high temperature treatment. It can be seen from Fig. 5a that when the temperature is set at 450 °C, the surface of the sample is scattered due to oxidation, but the overall dendritic skeleton morphology remains unchanged. When the heat treatment temperature increased to 550 °C, the branches of dendritic Sn particles gathered together and a large number of micropores appeared on the surface with the intensification of the oxidation degree (Fig. 5b). When the temperature reaches 600 °C, it can be seen from Fig. 5c that the dendritic morphology of the sample becomes less obvious, and the surface tends to be loose and porous. In summary, it can be concluded that the morphology of the Sn particles obtained by the electrochemical method changes from a regular dendritic structure to a loose and porous structure after different high-temperature treatments, which provides abundant catalytic active sites for the obtained samples as photocatalysts [40, 41].

To analyze the crystal structure and phase composition of the as-prepared samples after high-temperature treatment, XRD was carried out. The XRD patterns of the as-prepared products are shown in Fig. 5d. For the obtained Sn particles, all the diffraction peaks are in well agreement with the literature values of the tetragonal phase of metallic Sn (JCPDS

Fig. 4 SEM images of the Sn microparticles obtained at 15 V with different reaction time (a) 5 min, (b) 30 min, (c) 60 min and (d) 90 min



No.04–0673) [42–44]. Nearly no other peaks of impurities are detected, showing that the obtained Sn particles are of high purity. After Sn microparticles are treated at different high temperatures (450 °C, 550 °C and 600 °C), the peaks of cassiterite SnO₂ (JCPDS file No. 41–1445) can be also found in the patterns [45–47]. Therefore, the main component of the sample obtained after high temperature treatment is the hybrid compound composed of Sn and n-type semiconductor SnO₂ (Sn/SnO₂). It is worth noting that with the increase of heat treatment temperature, the diffraction peak of metal Sn in the hybrid gradually weakens, and the characteristic peak of SnO₂ gradually increases, indicating that the oxidation degree of Sn particles deepens with the increase of temperature.

3.4 Photocatalytic performance of Sn/SnO₂

N-type semiconductor SnO₂ has excellent stability and photocatalytic activity [48–50]. In this work, the Sn/SnO₂ hybrid with metal Sn-doped semiconductor SnO₂ properties obtained by high-temperature treatment of dendritic Sn particles can further improve the photocatalytic performance of traditional catalyst SnO₂ [51, 52]. To eliminate the effect of adsorption on photocatalysis, for each experiment, 50 mg of catalyst powder was added to 50 mL of RhB solution and stirred for 1 h in the dark to obtain adsorption/desorption equilibrium [53]. During light irradiation, the catalyst was kept in suspension by a magnetic stirrer, and 2 ml of the reaction solution was aspirated with a pipette every 30 min

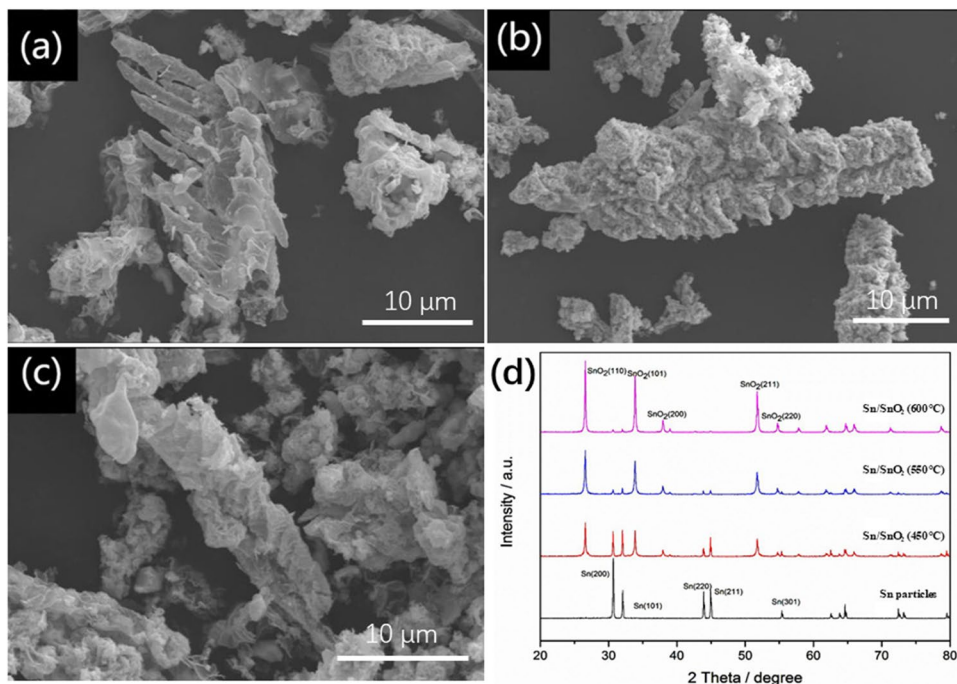
and centrifuged immediately to separate the catalyst from the solution. Finally, the concentration of RhB in the solution after a fixed time was measured at a wavelength of 554 nm by a UV–visible spectrophotometer [54]. The specific degradation efficiency calculation formula is as follows [55]:

$$\text{The degradation efficiency} = [(C_0 - C_t) / C_0] \times 100\% \quad (5)$$

where C_0 is the initial concentration of RhB, C_t is the concentration of RhB at time t . From Fig. 6a, after illumination for 5 h, compared with commercial SnO₂, the photocatalytic efficiency of the Sn/SnO₂ hybrid obtained in this work has been greatly improved, especially for the degradation efficiency of the catalyst obtained by calcination at 550 °C as high as 89.8%. It is worth noting that when the calcination temperature continues to increase to 600 °C, the photocatalytic efficiency of the hybrids decreases, which may be related to the electron mismatch in the Sn and SnO₂ heterojunction.

In order to verify the accuracy of the above photocatalytic efficiency and predict that the degradation of RhB by the catalyst may be related to the rapid interfacial transfer of photogenerated charge carriers and the subsequent effective charge separation, the photocurrent response behavior of the sample electrode in 0.1 M Na₂SO₄ electrolyte under intermittent visible light irradiation was tested using a three-electrode system in an electrochemical workstation [56, 57]. As shown in Fig. 6b, the prepared electrodes of different samples have a very obvious change in the response current under the condition of intermittent switching of the xenon

Fig. 5 SEM images of the Sn/SnO₂ microparticles obtained with different calcination temperature (a) 450 °C, (b) 550 °C and (c) 600 °C, (d) XRD patterns of Sn particles and Sn/SnO₂ products prepared with different calcination temperature



lamp for 15 s. The Sn/SnO₂ (550 °C) electrode demonstrated a stronger transient photocurrent response (0.38 mA/cm²) under visible light illumination, which was higher than that of commercial SnO₂ (0.26 mA/cm²), Sn/SnO₂ (450 °C) (0.33 mA/cm²), and Sn/SnO₂ (600 °C) (0.36 mA/cm²). In addition, after three cycles of light cycles, the current density under light conditions is basically constant, which proves that the prepared catalyst has good stability.

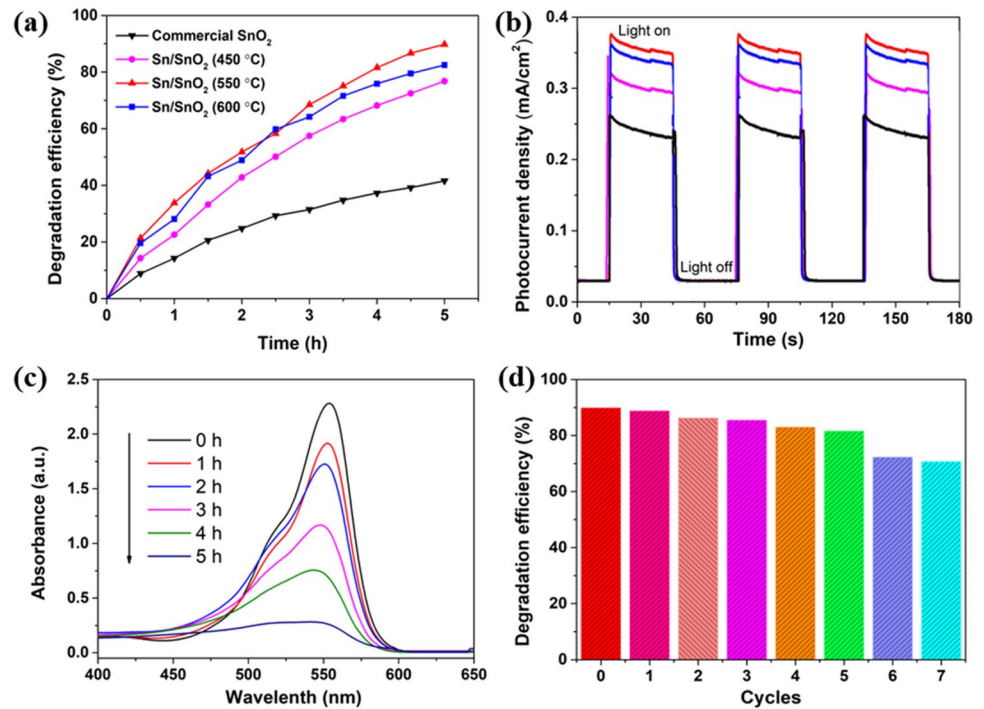
In order to more directly reflect the photocatalytic performance of the catalyst on RhB in different time periods, the time-dependent UV–vis absorption spectrum of RhB with Sn/SnO₂ (550 °C) electrode is also operated and shown in Fig. 6c. It can be clearly seen from the figure that with the passage of degradation time, the UV–vis absorption peak intensity of RhB in the solution decreased significantly at 554 nm. The recycling performance of photocatalysts is considered to be a key factor for evaluating the green sustainable catalysts, by repeated centrifugation, collecting and drying samples, the cyclic experiments of Sn/SnO₂ (550 °C) are conducted for seven runs and the result is depicted in Fig. 6d. After the first measurement, the catalyst is centrifuged, washed three times with deionized water and ethanol, and dried for the next cycle experiment. From the experimental results, it can be found that the degradation efficiency of the catalyst Sn/SnO₂ (550 °C) to RhB can still achieve more than 80.0% after 5 cycles, and the degradation efficiency decreases but still remains above 70.0% after 7 cycles. The degradation of performance may be related to the surface deactivation caused by the adsorption of RhB degradation products to the surface of the catalyst. Therefore, these

results indicate that the photocatalyst obtained in this study has good reusability.

3.5 Photocatalytic mechanism of Sn/SnO₂

The above results indicate that the Sn doped SnO₂ samples have shown much improved photocatalytic activity on the photodegradation of RhB than the pure commercial SnO₂. The UV–vis diffuse reflectance spectra of the pure SnO₂ and calcined sample Sn/SnO₂ are showed in Fig. 7a, it can be clearly seen that Sn/SnO₂ have good light absorption than pure SnO₂ in the visible light absorption range with a range of 400–750 nm, which indicates that doped Sn enhanced significantly visible light absorption of SnO₂ catalyst. The direct band gap (E_g) values of different catalysts are estimated from the $(Ah\nu)^2$ versus photon energy ($h\nu$) plot [$(Ah\nu)^2 = K(h\nu - E_g)$, where A is the absorption coefficient, $h\nu$ is the photon energy, K is a proportionality constant and E_g is the band gap energy for direct transitions] as showed in the Fig. 7b [58]. As depicted in Fig. 7b, the band gap of Sn/SnO₂ have been narrowed from 3.85 eV (pure SnO₂) to 3.82 eV (calcined at 450 °C), 3.76 eV (calcined at 550 °C) and 3.80 eV (calcined at 600 °C), respectively. It is worth mentioning that the band gap of samples obtained at 550 °C is the lowest and the photocatalytic effect is the best. The surface is attributed to the unique morphology to provide abundant active sites. The deep theory is that the appropriate amount of Sn-doped SnO₂ catalyst obtained at 550 °C promotes the transfer of photogenerated charge and extends the lifespan of photogenerated charge. Combined with the test results in Fig. 6b, Sn/

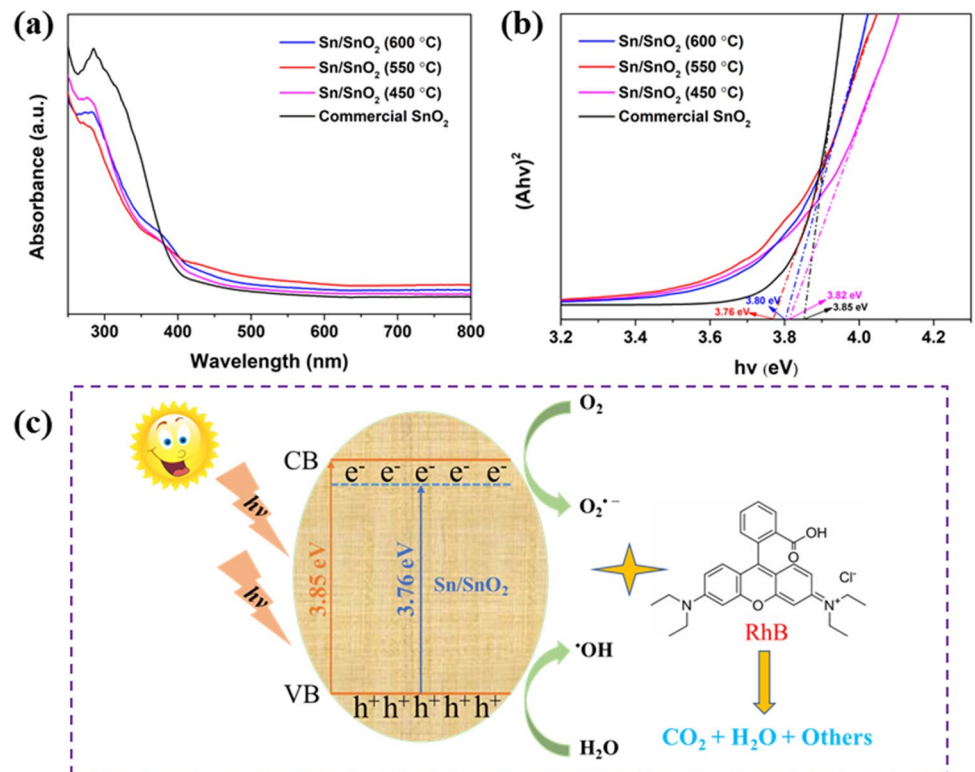
Fig. 6 (a) Degradation efficiency of RhB with various catalysts, (b) The photocurrent density of various catalysts, (c) The absorption spectra of RhB with Sn/SnO₂ (550 °C) as photocatalyst in different reaction time, and (d) The cycles of photocatalytic experiment of Sn/SnO₂ (550 °C) for RhB degradation



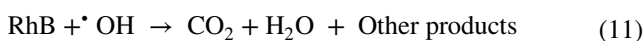
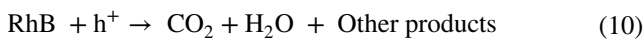
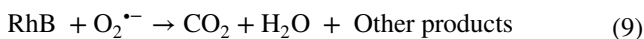
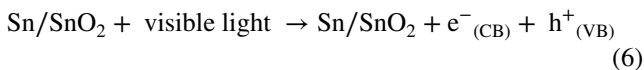
SnO₂ (550 °C) has excellent photocurrent response intensity, indicating that photogenerated electrons and holes are effectively separated, so that more active groups can participate in photocatalytic degradation.

The probable photocatalytic mechanism of Sn-doped SnO₂ hierarchical structures for degradation of RhB and schematic electronic structure for significantly improving photocatalytic performance are illustrated in Fig. 7c. Under

Fig. 7 (a) UV–Vis spectra and (b) plots of $(Ah\nu)^2$ vs. $h\nu$ of different catalysts, (c) Photoresponse mechanism of the Sn-doped SnO₂ (550 °C)



visible light excitation, electrons in the valence band (VB) of Sn-doped SnO₂ catalyst can be excited to the conduction band (CB) of the catalyst, while forming the same number of holes in VB (Eqs. (6)), leading to the formation of photogenerated electron–hole pairs [59, 60]. Compared to pure SnO₂, the Sn-doped SnO₂ hierarchical structure shows the stronger light absorption and lower band gap, therefore, more charge carriers can be excited in the process and then participate in following photocatalytic reactions [61, 62]. The reactive electrons (e⁻) from the Sn/SnO₂ reduce O₂ to O₂^{•-} (Eqs. (7)) [63]. Meanwhile, the reactive holes (h⁺) oxidize RhB to its radical cation either directly (Eqs. (10)) or through a primarily formed [•]OH produced by the oxidation of ubiquitous water (Eqs. (8)) [64, 65]. O₂^{•-} and [•]OH are proven to be the main active species, which can eventually convert organic dyes (RhB) into CO₂, H₂O and others (Eqs. (9) and (11)) [66].



4 Conclusions

Sn microparticles with dendritic structure were successfully synthesized from the cathode via a simple electrochemical method. It was found through SEM that the morphology and size of Sn particles were related to the experimental parameters, including composition of electrolyte (fluoride ion content, deionized water content), applied voltage, and reaction time. Then dendritic Sn particles were subjected to high-temperature calcination to obtain products that not only had numerous microporous morphologies, but also contained hybrid phases of Sn and SnO₂. The abundant catalytic active sites on the surface of the product and the characteristics of Sn-doped P-type semiconductor SnO₂ make it an excellent photocatalyst. Especially, when the calcination temperature is 550 °C, the Sn/SnO₂ product shows superior photocatalytic activity to other samples toward the degradation of RhB. In conclusion, this work provides a new strategy for the effective degradation of architecture and industrial dyes by a simple electrochemical method.

Acknowledgements The authors extend their appreciation to Taif University, Saudi Arabia for supporting this work through project number (TU-DSPP-2024-01).

Author contribution Yukun Lu prepared the materials and conducted most of the measurements and data analysis. Yaojie Zhang and Jiale Zhang contributed to the data analysis. Zhaoyang Li, Feiyang Hu and Duo Pan conceived the idea, wrote the paper, and coordinated the overall project. Saad Melhi and Xuetao Shi revised the paper. Mohammed A. Amin provided supervision and resources. Zeinhom M. El-Bahy reviewed and revised the manuscript. Qian Shao revised the manuscript and coordinated the overall project. All authors reviewed the manuscript.

Funding The research was funded by Taif University, Taif, Saudi Arabia (TU-DSPP-2024-01).

Data availability The authors confirm that the data supporting the findings of this study are available within the article. Raw data that support the findings of this study are available from the corresponding author, upon reasonable request.

Declarations

Competing interests The authors declare no competing interests.

References

- Bhat M, MR A, SV M, Das S, Roymahapatra G (2023) Photocatalytic degradation of dyes by titania/ferric oxide/polyvinyl alcohol nanocomposites. *ES Gen* 2:981. <https://doi.org/10.30919/esg981>
- Kumar A, Singh M, Bhatt N, Jayaswal P, Sethi M, Burcar E, Wang Z (2024) The perils of heavy metal contamination in groundwater: impacts on human health in the northeastern region of Jhunjhunu, Rajasthan. *ES Food Agrofor* 6:1079. <https://doi.org/10.30919/esfaf1079>
- Hou K, Xu X, Xiang Y, Chen X, Lam SS, Naushad M, Sonne C, Ge S (2023) Rapid uptake of gold ions by sulfonated humic acid modified phenolic resin with high adsorption capacity and selectivity. *Adv Compos Hybrid Mater* 6:77. <https://doi.org/10.1007/s42114-023-00647-y>
- Zhang H, Wang Z, Zhao Y, Cui W, Zhang X, Wang S, Walter ED, Sassi MJ, Pearce CI, Clark SB, Rosso KM (2023) Metal ion (Cr³⁺, Eu³⁺, UO₂²⁺) adsorption on gibbsite nanoplates. *Eng Sci* 4:896. <https://doi.org/10.30919/es896>
- Balasubramaniyan S, Khan HA, Swaminathan M (2023) Microbial and solar photocatalytic degradation of pyridine. *ES Energy Environ* 22:971. <https://doi.org/10.30919/esee971>
- Jasmine J, Ponvel KM (2023) Synthesis of Ag₂CdS₂/carbon nanocomposites for effective solar-driven ddy photodegradation and electrochemical application. *ES Energy Environ* 20:898. <https://doi.org/10.30919/esee898>
- Ansari MZ, Ansari SA, Kim S-H (2022) Fundamentals and recent progress of Sn-based electrode materials for supercapacitors: A comprehensive review. *J Energy Storage* 53:105187. <https://doi.org/10.1016/j.est.2022.105187>
- Shelke HD, Mohite AA, Torane AP, Madhale KV, Lokh CD (2022) Effect of Cu₄SnS₄ Layer Thickness on the Photovoltaic Parameters of Photoelectrochemical Solar Cells. *ES Materi. Manuf* 18:66–76. <https://doi.org/10.30919/esmm5f724>
- Ahmad I, Idress A, Assiri MA, Ahmed SB, Shaban M, Ghadi YY (2023) Sn-based materials in photocatalysis: A review. *Adv Colloid Interface Sci* 321:103032. <https://doi.org/10.1016/j.surfcoat.2018.10.011>

10. Le Caër G, Matteazzi P, Fultz B (1992) A microstructural study of mechanical alloying of Fe and Sn powders. *J Mater Res* 7:1387–1395. <https://doi.org/10.1557/JMR.1992.1387>
11. Xiaohui W, Zhiliang L, Jie Z, Xingguo L, Zujin S (2017) Arc-discharge synthesis of dual-carbonaceous-layer-coated tin nanoparticles with tunable structures and high reversible lithium storage capacity. *J Mater Chem A* 5:13769–13775. <https://doi.org/10.1039/C7TA03323K>
12. Zaikovskii A, Novopashin S, Maltsev V, Kardash T, Shundrina I (2019) Tin–carbon nanomaterial formation in a helium atmosphere during arc-discharge. *RSC Adv* 9:36621–36630
13. Pintar A, Batista J, Mušević I (2004) Palladium-copper and palladium-tin catalysts in the liquid phase nitrate hydrogenation in a batch-recycle reactor. *Appl Catal B* 52:49–60. <https://doi.org/10.1039/C9RA05485E>
14. Deb NK, Kalita K, Giri PK, Abhilash S, Umapathy G, Biswas R, Das A, Kabiraj D, Chopra S, Bhuyan M (2020) Carbon-backed thin tin (^{116}Sn) isotope target fabrication by physical vapor deposition technique. *J Radioanal Nucl Chem* 326:97–104. <https://doi.org/10.1007/s10967-020-07316-0>
15. Meléndrez M, Cárdenas G, Díaz VJ, Cruzat CC, Arbiol J (2009) Synthesis and aggregation study of tin nanoparticles and colloids obtained by chemical liquid deposition. *Colloid Polym Sci* 287:13–22. <https://doi.org/10.1007/s00396-008-1950-7>
16. Rozovskis G, Mockus Z, Pautienien V, Survila A (2002) Electrochemical determination of Sn (IV)/Sn(II) ratio in tin sol formed in copper–tin sulphate solution containing laprol 2402C. *Electrochem Commun* 4:76–79. [https://doi.org/10.1016/S1388-2481\(01\)00277-6](https://doi.org/10.1016/S1388-2481(01)00277-6)
17. Poinern GE, Ng Y-J, Fawcett D (2010) Fine-tuning of catalytic tin nanoparticles by the reverse micelle method for direct deposition of silicon nanowires by a plasma-enhanced chemical vapour technique. *J Colloid Interf Sci* 352:259–264. <https://doi.org/10.1016/j.jcis.2010.08.085>
18. Chee S-S, Lee J-H (2014) Synthesis of sub-10-nm Sn nanoparticles from Sn(II) 2-ethylhexanoate by a modified polyol process and preparation of AgSn film by melting of the Sn nanoparticles. *Thin Solid Films* 562:211–217. <https://doi.org/10.1016/j.tsf.2014.04.061>
19. Chaudhari Y, Tarkas H, Tak S, Punde A, Shah S, Rahane S, Waghmare A, Hase Y, Sali J, Jadkar S (2022) Influence of Mixed-solvent System and Reaction Temperature on In situ, Surfactant-free Synthesis of P3HT:SnS Nanocomposites. *ES Mater Manuf* 18:45–55. <https://doi.org/10.30919/esmm5f726>
20. Biswas S, Doherty J, Saladukha D, Ramasse Q, Majumdar D, Upmanyu M, Singha A, Ochalski T, Morris MA, Holmes JD (2016) Non-equilibrium induction of tin in germanium: towards direct bandgap $\text{Ge}_{1-x}\text{Sn}_x$ nanowires. *Nat Commun* 7:1–12. <https://doi.org/10.1038/ncomms11405>
21. Brumbach M, Veneman PA, Marrikar FS, Schulmeyer T, Simmonds A, Xia W, Lee P, Armstrong NR (2007) Surface composition and electrical and electrochemical properties of freshly deposited and acid-etched indium tin oxide electrodes. *Langmuir* 23:11089–11099. <https://doi.org/10.1021/la701754u>
22. Brande PV, Weymeersch A (2000) Steel coating by self-induced ion plating, a new high throughput metallization ion plating technique. *J Vac Sci Technol* 18:1555–1560. <https://doi.org/10.1116/1.582384>
23. Veeraraghavan B, Durairajan A, Haran B, Popov B, Guidotti R (2002) Study of Sn-coated graphite as anode material for secondary lithium-ion batteries. *J Electrochem Soc* 149:A675. <https://doi.org/10.1149/1.1470653>
24. Rokade A, Tarkas H, Rokade A, Waman V, Upasani D, Sali JV, Jadkar SR (2023) Effect of Incorporation of SnS Nanorods on the Growth Mechanism, Crystallinity, Optoelectronic Performance, and Stability of $\text{CH}_3\text{NH}_3\text{PbI}_3$ Perovskite Active Layer. *ES Mater. Manuf.* 22:937. <https://doi.org/10.30919/esmm937>
25. Kadam V, Jagtap C, Kumkale V, Rednam U, Lokhande P, Pathan H (2024) Photocatalytic degradation of rose bengal dye using chemically synthesized pristine and molybdenum doped zinc oxide. *Eng Sci* 8:1077. <https://doi.org/10.30919/es1077>
26. Sagadevan S, Lett JA, Weldegebrerial GK, Imteyaz S, Johan MR (2021) Synthesis, characterization, and photocatalytic activity of PPy/SnO₂ nanocomposite. *Chem Phys Lett* 783:139051. <https://doi.org/10.1016/j.cplett.2021.139051>
27. Arif HS, Murtaza G, Hanif H, Ali HS, Yaseen M, Khalid N (2017) Effect of La on structural and photocatalytic activity of SnO₂ nanoparticles under UV irradiation. *J Environ Chem Eng* 5:3844–3851. <https://doi.org/10.1016/j.jece.2017.07.043>
28. Abdelkader E, Nadja L, Naceur B, Noureddine B (2016) SnO₂ foam grain-shaped nanoparticles: Synthesis, characterization and UVA light induced photocatalysis. *J Alloy Compound* 679:408–419. <https://doi.org/10.1016/j.jallcom.2016.04.016>
29. Dhanalakshmi M, Saravanakumar K, Prabavathi SL, Abinaya M, Muthuraj V (2018) Fabrication of novel surface plasmon resonance induced visible light driven iridium decorated SnO₂ nanorods for degradation of organic contaminants. *J Alloy Compound* 763:512–524. <https://doi.org/10.1016/j.jallcom.2018.05.340>
30. Li X, Yan J, Zhu K (2021) Fabrication and Characterization of Pt doped Ti/Sb-SnO₂ Electrode and its Efficient Electro-Catalytic Activity toward Phenol. *Eng. Sci* 15:38–46. <https://doi.org/10.30919/es8d432>
31. Elango G, Kumaran SM, Kumar SS, Muthuraja S, Roopan SM (2015) Green synthesis of SnO₂ nanoparticles and its photocatalytic activity of phenolsulfonphthalein dye. *Spectrochim Acta Part A* 145:176–180. <https://doi.org/10.1016/j.saa.2015.03.033>
32. Drouiche N, Aoudj S, Hecini M, Ghaffour N, Lounici H, Mameri N (2009) Study on the treatment of photovoltaic wastewater using electrocoagulation: Fluoride removal with aluminium electrodes—Characteristics of products. *J Hazard Mater* 169:65–69. <https://doi.org/10.1016/j.jhazmat.2009.03.073>
33. Allam NK, Grimes CA (2011) Electrochemical fabrication of complex copper oxide nanoarchitectures via copper anodization in aqueous and non-aqueous electrolytes. *Mater Lett* 65:1949–1955. <https://doi.org/10.1016/j.matlet.2011.03.105>
34. Deen K, Farooq A, Raza M, Haider W (2014) Effect of electrolyte composition on TiO₂ nanotubular structure formation and its electrochemical evaluation. *Electrochim Acta* 117:329–335. <https://doi.org/10.1016/j.electacta.2013.11.108>
35. Su JF, Kuan W-F, Liu H, Huang C (2019) Mode of electrochemical deposition on the structure and morphology of bimetallic electrodes and its effect on nitrate reduction toward nitrogen selectivity. *Appl Catal B: Environ* 257:117909. <https://doi.org/10.1016/j.apcatb.2019.117909>
36. Zhang X, Wan K, Subramanian P, Xu M, Luo J, Fransær J (2020) Electrochemical deposition of metal–organic framework films and their applications. *J Mater Chem A* 8:7569–7587. <https://doi.org/10.1039/D0TA00406E>
37. McKaveney JP, Byrnes C (1970) Apparatus using semiconductor electrodes for the measurement of acid concentrations. *Anal Chem* 42:1023–1028. <https://doi.org/10.1021/ac60291a018>
38. Han Z, Niu Y, Shi X, Pan D, Liu H, Qiu H, Chen W, Xu BB, El-Bahy ZM, Hou H, Elsharkawy ER, Amin MA, Liu C, Guo Z (2024) MXene@c-MWCNT adhesive silica nanofiber membranes enhancing electromagnetic interference shielding and thermal insulation performance in extreme environments. *Nano-Micro Lett* 16:195. <https://doi.org/10.1007/s40820-024-01398-1>
39. Sun B, Zhou G, Zhang Y, Liu R, Li T (2015) Photocatalytic properties of exposed crystal surface-controlled rutile TiO₂ nanorod

- assembled microspheres. *Chem Eng J* 264:125–133. <https://doi.org/10.1016/j.cej.2014.11.070>
40. Pan D, Ge S, Zhao J, Shao Q, Guo L, Zhang X, Lin J, Xu G, Guo Z (2018) Synthesis, characterization and photocatalytic activity of mixed-metal oxides derived from NiCoFe ternary layered double hydroxides. *Dalton Trans* 47:9765–9778. <https://doi.org/10.1039/C8DT01045E>
 41. Gu Y, Pan Z, Zhang H, Zhu J, Yuan B, Pan D, Wu C, Dong B, Guo Z (2020) Synthesis of high performance diesel oxidation catalyst using novel mesoporous AlLaZrTiOx mixed oxides by a modified sol-gel method. *Adv Compos Hybrid Mater* 3:583–593. <https://doi.org/10.1007/s42114-020-00193-x>
 42. Wu L, Hu X, Qian J, Pei F, Wu F, Mao R, Ai X, Yang H, Cao Y (2013) A Sn–SnS–C nanocomposite as anode host materials for Na-ion batteries. *J Mater Chem A* 1:7181–7184. <https://doi.org/10.1039/C3TA10920H>
 43. Wu L, Lu H, Xiao L, Qian J, Ai X, Yang H, Cao Y (2014) A tin (ii) sulfide–carbon anode material based on combined conversion and alloying reactions for sodium-ion batteries. *J Mater Chem A* 2:16424–16428. <https://doi.org/10.1039/C4TA03365E>
 44. Zhang N, Zhao Q, Han X, Yang J, Chen J (2014) Pitaya-like Sn@C nanocomposites as high-rate and long-life anode for lithium-ion batteries. *Nanoscale* 6:2827–2832. <https://doi.org/10.1039/C3NR05523J>
 45. Guo Y, Tan R, Li Y, Song W (2012) Solution route to SnO₂ crystals with controllable morphology. *Appl Surf Sci* 258:1958–1963. <https://doi.org/10.1016/j.apsusc.2011.06.037>
 46. Wang WW, Zhu YJ, Yang LX (2007) ZnO–SnO₂ hollow spheres and hierarchical nanosheets: hydrothermal preparation, formation mechanism, and photocatalytic properties. *Adv Funct Mater* 17:59–64. <https://doi.org/10.1002/adfm.200600431>
 47. Cheng B, Russell JM, Shi W, Zhang L, Samulski ET (2004) Large-scale, solution-phase growth of single-crystalline SnO₂ nanorods. *J Am Chem Soc* 126:5972–5973. <https://doi.org/10.1021/ja0493244>
 48. Derikvandi H, Nezamzadeh-Ejehieh A (2017) Synergistic effect of pn heterojunction, supporting and zeolite nanoparticles in enhanced photocatalytic activity of NiO and SnO₂. *J Colloid Interf Sci* 490:314–327. <https://doi.org/10.1016/j.jcis.2016.11.069>
 49. Kim SP, Choi MY, Choi HC (2016) Photocatalytic activity of SnO₂ nanoparticles in methylene blue degradation. *Mater Res Bull* 74:85–89. <https://doi.org/10.1016/j.materresbull.2015.10.024>
 50. Kawade AN, Bhujbal PK, Supekar AT, Sonawane KM, Pathan HM, Shaikh SF, Al-Kaitani AAA (2021) Comparative Study of Eosin-Y and Rose Bengal Sensitized SnO₂-ZnO Composite Electrode for Dye-Sensitized Solar Cell. *ES Energy Environ* 14:73–78. <https://doi.org/10.30919/eesec8c495>
 51. Roy S, Luitel H, Sanyal D (2019) Magnetic properties of transition metal doped SnO₂: A detailed theoretical study. *Computat Condens Matte* 21:e00393. <https://doi.org/10.1016/j.cocom.2019.e00393>
 52. Soitah TN, Yang C, Sun L (2010) Structural, optical and electrical properties of Fe-doped SnO₂ fabricated by sol–gel dip coating technique. *Mat Sci Semicon Proc* 13:125–131. <https://doi.org/10.1016/j.mssp.2010.03.002>
 53. Pan D, Ge S, Zhao J, Tian J, Shao Q, Guo L, Mai X, Wu T, Murugadoss V, Liu H (2018) Synthesis and characterization of ZnNiIn layered double hydroxides derived mixed metal oxides with highly efficient photoelectrocatalytic activities. *Ind Eng Chem Res* 58:836–848. <https://doi.org/10.1021/acs.iecr.8b04829>
 54. Kumar R, Umar A, Kumar R, Chauhan M, Kumar G, Chauhan S (2021) Spindle-like Co₃O₄-ZnO nanocomposites scaffold for hydrazine sensing and photocatalytic degradation of rhodamine B dye. *Eng. Sci* 16:288–300. <https://doi.org/10.30919/es8d548>
 55. Zhang F, Cheng W, Yu Z, Ge S, Shao Q, Pan D, Liu B, Wang X, Guo Z (2021) Microwave hydrothermally synthesized WO₃/UiO-66 nanocomposites toward enhanced photocatalytic degradation of rhodamine B. *Adv Compos Hybrid Mater* 4:1330–1342. <https://doi.org/10.1007/s42114-021-00346-6>
 56. Sun Z, Zhang Y, Guo S, Shi J, Shi C, Qu K, Qi H, Huang Z, Murugadoss V, Huang M, Guo Z (2022) Confining FeNi nanoparticles in biomass-derived carbon for effectively photo-Fenton catalytic reaction for polluted water treatment. *Adv Compos Hybrid Mater* 5:1566–1581. <https://doi.org/10.1007/s42114-022-00477-4>
 57. Xu Z, Yu J (2011) Visible-light-induced photoelectrochemical behaviors of Fe-modified TiO₂ nanotube arrays. *Nanoscale* 3:3138–3144. <https://doi.org/10.1039/C1NR10282F>
 58. Huang K, Zhang Q, Yang F, He D (2010) Ultraviolet photoconductance of a single hexagonal WO₃ nanowire. *Nano Res* 3:281–287. <https://doi.org/10.1007/s12274-010-1031-3>
 59. Shinde DR, Quraishi IS, Pawar RA (2021) An efficient visible light driven photocatalytic removal of dyes from the dye effluent using metal halide lamp based slurry reactor. *ES Energy Environ* 14:54–62. <https://doi.org/10.30919/eesec8c504>
 60. Pan D, Ge S, Zhang X, Mai X, Li S, Guo Z (2018) Synthesis and photoelectrocatalytic activity of In₂O₃ hollow microspheres via a bio-template route using yeast templates. *Dalton Trans* 47:708–715. <https://doi.org/10.1039/C7DT03878J>
 61. Khan SH, Pathak B, Fulekar MH (2020) A study on the influence of metal (Fe, Bi, and Ag) doping on structural, optical, and antimicrobial activity of ZnO nanostructures. *Adv Compos Hybrid Mater* 3:551–569. <https://doi.org/10.1007/s42114-020-00174-0>
 62. Sun D, Jang S, Yim SJ, Ye L, Kim DP (2018) Metal Doped Core-Shell Metal-Organic Frameworks@ Covalent Organic Frameworks (MOFs@COFs) Hybrids as a Novel Photocatalytic Platform. *Adv Funct Mater* 28:1707110. <https://doi.org/10.1002/adfm.201707110>
 63. Xu T, Zhang L, Cheng H, Zhu Y (2011) Significantly enhanced photocatalytic performance of ZnO via graphene hybridization and the mechanism study. *Appl Catal B: Environ* 101:382–387. <https://doi.org/10.1016/j.apcatb.2010.10.007>
 64. Wang W-L, Wu Q-Y, Huang N, Xu Z-B, Lee M-Y, Hu H-Y (2018) Potential risks from UV/H₂O₂ oxidation and UV photocatalysis: a review of toxic, assimilable, and sensory-unpleasant transformation products. *Water Res* 141:109–125. <https://doi.org/10.1016/j.watres.2018.05.005>
 65. Song Y, Tian J, Gao S, Shao P, Qi J, Cui F (2017) Photodegradation of sulfonamides by g-C₃N₄ under visible light irradiation: effectiveness, mechanism and pathways. *Appl Catal B: Environ* 210:88–96. <https://doi.org/10.1016/j.apcatb.2017.03.059>
 66. Xie K, Wei S, Alhadhrami A, Liu J, Zhang P, Elnaggar AY, Zhang F, Mahmoud MHH, Murugadoss V, El-Bahy SM, Wang F, Li C, Li G (2022) Synthesis of CsPbBr₃/CsPb₂B₅@silica yolk-shell composite microspheres: precisely controllable structure and improved catalytic activity for dye degradation. *Adv Compos Hybrid Mater* 5:1423–1432. <https://doi.org/10.1007/s42114-022-00520-4>

Publisher's Note Springer Nature remains neutral with regard to jurisdictional claims in published maps and institutional affiliations.

Springer Nature or its licensor (e.g. a society or other partner) holds exclusive rights to this article under a publishing agreement with the author(s) or other rightsholder(s); author self-archiving of the accepted manuscript version of this article is solely governed by the terms of such publishing agreement and applicable law.

Authors and Affiliations

Yukun Lu¹ · Yaojie Zhang² · Jiale Zhang¹ · Zhaoyang Li¹ · Feiyang Hu³ · Duo Pan⁴ · Saad Melhi⁵ · Xuetao Shi⁶ · Mohammed A. Amin⁷ · Zeinhom M. El-Bahy⁸ · Qian Shao⁹

✉ Zhaoyang Li
lizhaoyang@squ.edu.cn

✉ Feiyang Hu
fyhu@jxau.edu.cn

✉ Duo Pan
panduonerc@zzu.edu.cn

¹ College of Architecture & Civil Engineering, Shangqiu Normal University, Shangqiu 476000, China

² College of Chemical Engineering, Ordos Institute of Technology, Ordos 017000, China

³ College of Chemistry and Materials, Jiangxi Agricultural University, Nanchang 330045, China

⁴ Key Laboratory of Materials Processing and Mold (Zhengzhou University), Ministry of Education, National Engineering Research Center for Advanced Polymer Processing Technology, Zhengzhou University, Zhengzhou 450002, China

⁵ Department of Chemistry, College of Science, University of Bisha, 61922 Bisha, Saudi Arabia

⁶ Shaanxi Key Laboratory of Macromolecular Science and Technology, School of Chemistry and Chemical Engineering, Northwestern Polytechnical University, Xi'an 710072, China

⁷ Department of Chemistry, College of Science, Taif University, P.O. Box 11099, 21944 Taif, Saudi Arabia

⁸ Department of Chemistry, Faculty of Science, Al-Azhar University, Nasr CityCairo 11884, Egypt

⁹ College of Chemical and Environmental Engineering, Shandong University of Science and Technology, Qingdao 266590, China